Liquid transport produced by a cluster of peristaltic contractions in a circular channel

Oyama, Tomoki
Ishida, Shunichi
Maeyama, Kohei
Miyagawa, Taimei
Imai, Yohsuke

(Citation)
Physical Review Fluids,6(9):093102

(Issue Date)
2021-09-28

(Resource Type)
journal article

(Version)
Version of Record

(URL)
https://hdl.handle.net/20.500.14094/90008698

Liquid transport produced by a cluster of peristaltic contractions in a circular channel

Tomoki Oyama,[1] Shunichi Ishida,[1] Kohei Maeyama,[1]
Taimei Miyagawa,[2] and Yohsuke Imai[1,*]
[1]*Graduate School of Engineering, Kobe University, Kobe 657-8501, Japan*
[2]*Graduate School of Science and Technology, Hirosaki University, Hirosaki 036-8561, Japan*

(Received 12 March 2021; accepted 15 September 2021; published 28 September 2021)

Clustered contractions are observed in the human small intestine after fatty meals or in patients with gastrointestinal diseases. We investigate flow produced by a cluster of peristaltic contractions propagating along a circular channel for a finite Reynolds number $\mathrm{Re} \sim 10^2$ and a finite contraction width (wavelength) $\lambda/D \sim 1$. We perform a computational fluid dynamics analysis of a Newtonian liquid using the cumulant lattice Boltzmann method where zero pressure is given to both ends of the channel. We show that clustered contractions cause retrograde flow over the cluster and fluid trapping in the upstream and downstream regions of the cluster. Flow rate is not proportional to the number of peristaltic waves in a cluster, in particular, for large contraction ratio (amplitude). To understand the underlying mechanism, we simulate flow produced by an isolated contraction in channels with different lengths. The magnitude of pressure gradient produced by the isolated contraction does not decrease largely with increasing the channel length, minimizing a decrease in flow rate. When flow rates of clustered contractions with different numbers of waves are plotted as a function of the channel length per wave, the flow rates collapse onto a single curve of each contraction ratio. In addition, the flow rates of the clustered contractions converge to the flow rates of infinitely periodic contractions. We also compare the characteristics of the flow rate for $\mathrm{Re} \sim 10^2$ and $\lambda/D \sim 1$ to those for $\mathrm{Re} \to 0$ and $\lambda/D \to \infty$.

DOI: 10.1103/PhysRevFluids.6.093102

I. INTRODUCTION

The gastrointestinal tract is the digestive organs consisting of the mouth, esophagus, stomach, small intestine, large intestine, and anus. In these organs, various wall movements are generated to transport, mix, and segment foods. There are several contractile patterns in the gastrointestinal tract. In the small intestine, for example, frequently occurring contractile patterns include peristaltic, stationary, and clustered contractions [1]. In peristaltic contractions, contraction waves propagate in the anterograde direction. The main role of peristaltic contractions is to transport foods. Stationary contractions are the alternating contraction, relaxation of the wall at the same site, and responsible for mixing and segmenting foods also called segmenting contractions. Clustered contractions are characterized by a cluster of several peristaltic contractions or segmenting contractions. In experimental studies on human subjects, a cluster of three–ten peristaltic waves was often defined as clustered contractions [2,3]. Clustered contractions are frequently observed after fatty meals in physiological conditions. For pathological conditions, clustered contractions are observed in

*yimai@mech.kobe-u.ac.jp

patients with obese [2], intestinal obstruction [3], irritable bowel syndrome [4–7] and Crohn's diseases [8,9].

It is difficult to observe gastrointestinal flows produced by peristaltic contractions in experiments. Theoretical and numerical studies have been conducted for peristaltic flows [10–20]. Shapiro *et al.* [10] presented an analytical solution of peristaltic flows for periodic and infinitely long waves in the Stokes flow regime using the lubrication theory. Jaffrin and Shapiro [11] summarized basic properties of flows generated by periodic peristaltic waves in a two-dimensional channel. The basic flow patterns include the transport, reflux, and trapping of fluids, where the reflux is a phenomenon of moving contents backward, and the fluid trapping is caused by stagnation points. Takabatake and Ayukawa [12] calculated the velocity, pressure, and stress fields of peristaltic flows for various values of the Reynolds number (Re), contraction (wave) amplitude, and wavelength. They reported that the size and occurrence part of reflux change with the Reynolds number. Pozrikidis [13] investigated effects of the wavelength and wave amplitude on the trapping and reflux of peristaltic flows using a two-dimensional straight channel with periodic boundaries. For peristaltic waves with a short wavelength, mean flow rate first increases quadratically and then increases linearly with the wave amplitude of the peristaltic waves. For peristaltic waves with a middle wavelength, the mean flow rate increases almost linearly with the wave amplitude. It was also suggested that the trapping did not affect flow rate.

In this paper, we focus on clustered contractions in the gastrointestinal tract. Although there have been many studies on periodic waves or a single wave, few studies have been conducted on clustered waves. For example, Li and Brasseur [14] generalized the analytical solution proposed by Shapiro *et al.* [10] to study nonperiodic waves with arbitrary shapes in a finite length channel. They compared flows produced by a single expansion wave and clustered waves and showed that the reflux for the clustered waves behaves differently from the single expansion wave. However, the analytical solution based on the lubrication theory may not be applicable to physiological conditions of the gastrointestinal flows. Assuming that the diameter of the small intestine is $D = 20$–30 mm, the maximum peristaltic velocity is approximately $V = 30$ mm/s [21–23], and the viscosity of intestinal contents is $\mu = 10^{-3}$ Pa s (water and diarrhea, for example), the Reynolds number is estimated to be $\mathrm{Re} \sim 10^2$. In addition, the lubrication theory assumes an infinitely long wave $\lambda/D \to \infty$, where λ is the wavelength. Therefore, whereas clustered contractions are an important gastrointestinal motility in both physiological and pathological conditions, effects of clustered contractions on gastrointestinal flows are not fully understood. The purpose of this paper is to clarify liquid flow produced by clustered contractions in a circular and finite length channel for $\mathrm{Re} \sim 10^2$ and $\lambda/D \sim 1$. Although anatomically realistic geometries have been used in previous studies [24–27], we use a simplified geometry to gain a fundamental understanding of flows produced by peristaltic contractions. We perform a computational fluid dynamics analysis of a Newtonian liquid using the cumulant lattice Boltzmann method, where zero pressure is given to both the ends of the channel. We then discuss the relationship between clustered contractions and periodic contractions. We also compare the flow characteristics for $\mathrm{Re} = 10^2$ and $\lambda/D = 1$ to those for $\mathrm{Re} \to 0$ and $\lambda/D \to \infty$.

II. NUMERICAL METHODS

A. Geometry

Consider a three-dimensional circular channel with diameter D and length L. Clustered contractions consist of several peristaltic waves with an identical shape. Each peristaltic wave is characterized by the contraction ratio (amplitude) D_p/D, and the contraction width (wavelength) λ. The diameter of the lumen is given by

$$d(x,t) = \begin{cases} D - \frac{D_p}{2}\left\{1 + \cos\frac{2\pi}{\lambda}(x - x_{p,i} - Vt)\right\} & \left(-\frac{\lambda}{2} \leqslant x - x_{p,i} - Vt \leqslant \frac{\lambda}{2}\right), \\ D & (\text{otherwise}) \end{cases} \tag{1}$$

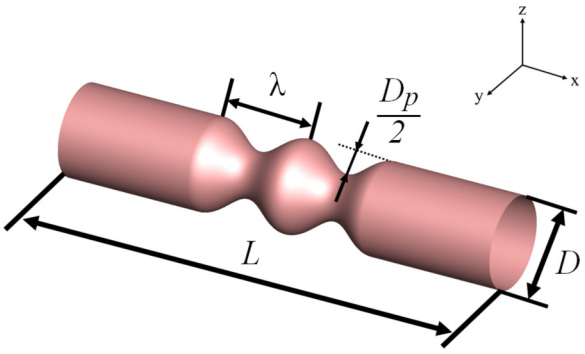

FIG. 1. Wall geometry for $N_p = 2$, where L is the channel length, D is the channel diameter, D_p is the contraction amplitude, and λ is the contraction width. The contraction ratio is given by D_p/D.

where V is the peristaltic velocity, x is the position along the channel length direction, $x_{p,i}$ is the initial position of the ith peristaltic wave, and t is the time. To prevent adjacent waves from overlapping, we set $x_{p,1} = \lambda/2$ and $x_{p,i+1} = x_{p,i} - \lambda$. The direction of wave propagation is the positive direction of x axis, and the cross sections at $x = -L/2$ and $x = L/2$ are called inlet and outlet, respectively. The peristaltic wave near the outlet is defined as the first wave. A wall geometry was shown in Fig. 1 for the number of peristaltic waves $N_p = 2$.

During the propagation of peristaltic waves, the wall deforms only in the radial direction, i.e., the direction of the wall velocity is the radial direction toward the center of the channel, and the wall velocity is zero in the propagation direction. The wall velocity $u_w(x,t)$ is obtained by the time derivative of $d(x,t)$ as

$$u_w(x,t) = \begin{cases} -\frac{\pi V D_p}{\lambda} \sin\frac{2\pi}{\lambda}(x - x_{p,i} - Vt) & \left(-\frac{\lambda}{2} \leqslant x - x_{p,i} - Vt \leqslant \frac{\lambda}{2}\right) \\ 0 & (\text{otherwise}) \end{cases}. \tag{2}$$

B. Fluid dynamics

An incompressible Newtonian liquid is considered for intestinal contents. To solve fluid dynamics, the lattice Boltzmann method [28] is employed. The time evolution of the distribution function f for the direction $i, j, k \in \{-1, 0, 1\}$ is given by the following collision and streaming steps:

$$f^*_{ijk}(\boldsymbol{x}, t) = f_{ijk}(\boldsymbol{x}, t) + \Omega(\boldsymbol{x}, t), \tag{3}$$

$$f_{ijk}(\boldsymbol{x} + \boldsymbol{c}_{ijk}\Delta t, t + \Delta t) = f^*_{ijk}(\boldsymbol{x}, t), \tag{4}$$

where f^* is the postcollision distribution function, $\boldsymbol{c}_{ijk} = (ic, jc, kc)$ is the discrete velocity, $c = \Delta x/\Delta t$, Δx is the lattice spacing, Δt is the discrete time, and Ω is the collision operator. In this paper, we use the cumulant collision model [29] for the stable computation in which the collision process is calculated in the cumulant space, and the distribution function f is transformed into the cumulant C as

$$C_{\alpha\beta\gamma} = c^{-\alpha-\beta-\gamma} \frac{\partial^\alpha \partial^\beta \partial^\gamma}{\partial \Xi^\alpha \partial \Upsilon^\beta \partial Z^\gamma} \ln[F(\boldsymbol{\Xi})]|_{\Xi=\Upsilon=Z=0}, \tag{5}$$

where $F(\boldsymbol{\Xi}) = \mathcal{L}[f]$ is the Laplace-transformed distribution function, $\boldsymbol{\Xi} = (\Xi, \Upsilon, Z)$ is the momentum wave number, and $\alpha, \beta, \gamma \in \{0\text{–}2\}$ are the indices of the cumulant. Note that the order of the cumulant is given by the sum of its indices $\alpha + \beta + \gamma$. The postcollision cumulant C^* is

calculated by

$$C^*_{\alpha\beta\gamma} = (1 - \omega_{\alpha\beta\gamma})C_{\alpha\beta\gamma} + \omega_{\alpha\beta\gamma}C^{eq}_{\alpha\beta\gamma}, \tag{6}$$

where $C^{eq}_{\alpha\beta\gamma}$ is the equilibrium cumulant and $\omega_{\alpha\beta\gamma}$ is the relaxation rate coefficient. The relaxation rate coefficients for the second-order cumulants are related to the kinematic viscosity ν; $\omega_{200} = \omega_{020} = \omega_{002} = \omega_{110} = \omega_{101} = \omega_{011} = 1/\tau$, where $\tau = 1/2 + \nu\,\Delta t/\Delta x^2$ is the relaxation time. The other relaxation rate coefficients are set to unity [29]. After the collision process of the cumulants, the postcollision distribution function f^* is obtained from C^* by applying the backward transformation of Eq. (5).

The fluid density ρ, velocity $\boldsymbol{u}$ and pressure p are calculated as

$$\rho(\boldsymbol{x}, t) = \sum_{ijk} f_{ijk}(\boldsymbol{x}, t), \tag{7}$$

$$\boldsymbol{u}(\boldsymbol{x}, t) = \frac{1}{\rho(\boldsymbol{x}, t)} \sum_{ijk} \boldsymbol{c}_{ijk} f_{ijk}(\boldsymbol{x}, t), \tag{8}$$

$$p(\boldsymbol{x}, t) = \frac{c^2 \rho(\boldsymbol{x}, t)}{3}. \tag{9}$$

The linear-interpolated bounce-back scheme [30] is used for the curved and moving wall boundary conditions. Zero-pressure boundary condition is applied to both the ends of the channel.

C. Analysis

In this paper, we mainly discuss numerical results for $\mathrm{Re} = 10^2$ where Re is defined by

$$\mathrm{Re} = \frac{\rho V D}{\mu}, \tag{10}$$

where ρ is the liquid density, V is the peristaltic velocity, D is the channel diameter, and μ is the liquid viscosity.

Computations are performed in a coordinate system moving with the peristaltic velocity V (moving frame) and computational results are transformed to a stationary coordinate system (stationary frame) to discuss the results.

To evaluate effects of clustered contractions on flow, we calculate the volume flow rate,

$$Q(t) = \int_S \boldsymbol{u}(\boldsymbol{x}, t)\cdot\boldsymbol{n}\, dS, \tag{11}$$

where S is the cross-sectional area of the outlet, $\boldsymbol{u}$ is the fluid velocity, and $\boldsymbol{n}$ is the unit normal vector perpendicular to the cross section. In this paper, we only consider a quasisteady flow field, and we terminate the computation when the mean flow rate is satisfied with

$$\left| \frac{Q\left(t + \frac{D}{V}\right) - Q(t)}{D^2 V} \right| < 10^{-6}. \tag{12}$$

D. Accuracy

To determine the lattice spacing Δx and the relaxation time τ (the time-step size Δt), we check the numerical accuracy. Because the lattice Boltzmann method is a weakly compressible scheme, the Mach number must be sufficiently small [28]. In this paper, the Mach number is $\mathrm{Ma} < 2.0 \times 10^{-2}$. We examine flow generated by an isolated peristaltic wave $N_p = 1$ for various values of Δx and τ, where $\mathrm{Re} = 10^2$, $D_p/D = 0.75$, $\lambda/D = 1$, and $L/D = 5$.

Flow rate at the quasisteady state is shown in Fig. 2(a) as a function of τ. Because of the memory size restriction on our computers, we were not able to check $\Delta x/D < 8 \times 10^{-3}$. However, for $\Delta x/D \leqslant 1.0 \times 10^{-2}$, the flow rate may converge to $Q/D^2V \sim 0.668$, and the flow rate does

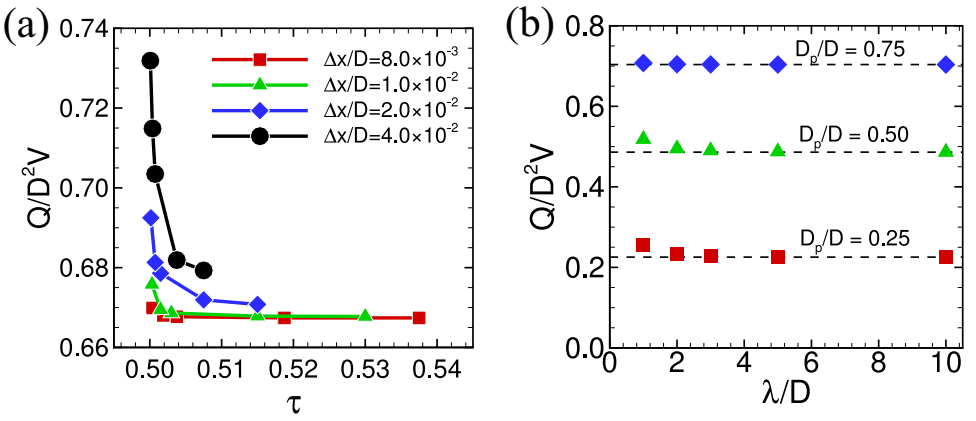

FIG. 2. (a) Effect of the lattice spacing Δx and the relaxation time τ on numerical result. Flow rate Q is shown for $N_p = 1$, $\mathrm{Re} = 10^2$, $D_p/D = 0.75$, $\lambda/D = 1$, and $L/D = 5$. (b) Flow rate of periodic waves for $\mathrm{Re} = 10^{-1}$ as a function of λ/D. Dashed lines show analytical solutions for $\mathrm{Re} \to 0$ and $\lambda/D \to \infty$ [10].

not depend on τ except for $\tau \sim 0.5$. In this paper, the lattice spacing is, therefore, fixed to $\Delta x/D = 1.0 \times 10^{-2}$, and the relaxation time is $\tau = 0.53$ ($\Delta t\, V/D = 10^{-4}$) for $\mathrm{Re} = 10^2$. For other Res, the relaxation time is fixed at $\tau = 0.8$.

Shapiro *et al.* [10] proposed an analytical solution for periodic and infinitely long waves ($\lambda/D \gg 1$) in the Stokes flow regime. To check the accuracy of our numerical method, we examine periodic waves with varying λ/D for $\mathrm{Re} = 0.1$ as shown in Fig. 2(b). The numerical results approach the analytical solution when $\lambda/D \gg 1$. Further comparison to $\mathrm{Re} \to 0$ and $\lambda/D \to \infty$ is presented in Sec. III E.

III. RESULTS AND DISCUSSION

A. Flow produced by clustered contractions

We first briefly show the effect of Re on flow rate produced by clustered contractions. Figure 3 shows the variation of flow rate with Re for three values of D_p/D, where $N_p = 2$, $L/D = 15$, and

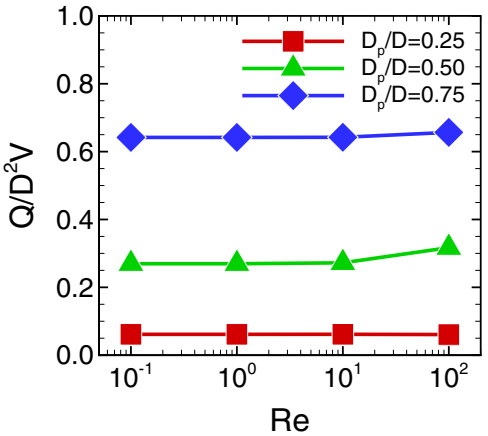

FIG. 3. Effect of Re on Q/D^2V for $N_p = 2$, $L/D = 15$, and $\lambda/D = 1$.

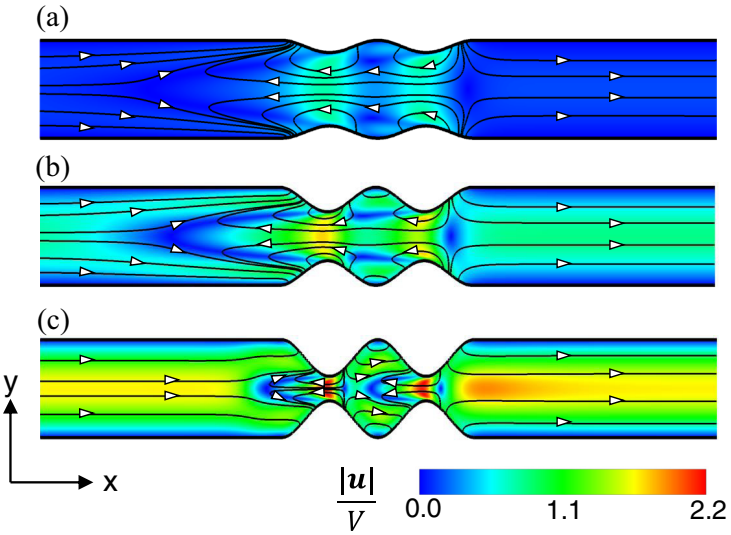

FIG. 4. Stationary frame streamlines with velocity magnitude at the channel center (x-y cross section) for $N_p = 2$, $L/D = 15$, and $\lambda/D = 1$: (a) $D_p/D = 0.25$; (b) $D_p/D = 0.50$; (c) $D_p/D = 0.75$. Contracted regions are magnified.

$\lambda/D = 1$. The flow rate is nearly the same for $\mathrm{Re} = 10^{-1}$–10^{1}, but it is slightly larger for $\mathrm{Re} = 10^{2}$ at $D_p/D = 0.5$ and 0.75.

Hereafter, we concentrate on the results of $\mathrm{Re} = 10^{2}$ and $\lambda/D = 1$. Figure 4 shows streamlines with velocity magnitude for $N_p = 2$. For all the contraction ratios examined in this paper, streamlines are asymmetric with respect to the clustered waves. The velocity direction at the most contracted region is opposite to the peristaltic wave propagation. The x-directional velocity u at the most contracted region of the first wave, and that at the widest region between the first and the second waves are shown in Fig. 5. For the most contracted region, the velocities are negative, and the position of the largest velocity magnitude is not the channel center but near the wall. For the widest region between the first and the second waves, the velocity profile is also not parabolic, and retrograde flow occurs near the channel center. The magnitude of the retrograde flow velocity is larger for $D_p/D = 0.5$ than the other cases. We also find in Fig. 4 that for $D_p/D = 0.25$ and 0.5, some streamlines depart from the downstream side of the first wave and arrive at the upstream side of the second wave, indicating long retrograde flow over the two waves. For $D_p/D = 0.75$, however, the long retrograde flow disappear. Retrograde flow over the cluster of three peristaltic waves is also found in $N_p = 3$. Note that retrograde flow over several peristaltic waves was not observed for periodic contractions in previous studies [13].

A famous phenomenon of peristaltic flows is fluid trapping [10]. Fluid trapping can be seen in streamlines at the wave frame shown in Fig. 6. For $D_p/D = 0.75$, fluid trapping occurs at the region between the first and the second waves. In addition, the trapping also occurs in the downstream and upstream regions of the clustered contractions (the straight regions ahead and behind the contractions). The tendency is the same for $N_p = 3$. A previous study on the Stokes flow [13] showed that fluid trapping occurs when the contraction amplitude increases. Another study showed that the trapping becomes asymmetric and decreases in size when Re increases [31]. The results of our paper are in good agreement with these previous studies. However, because the previous studies were conducted on periodic waves and had no straight regions in channels, the fluid trapping at the straight regions was not reported.

We next examine how flow rate changes with the number of peristaltic waves in clustered contractions. Figure 7 shows the normalized flow rate $Q/Q_{N_p=1}$ as a function of N_p, where $Q_{N_p=1}$

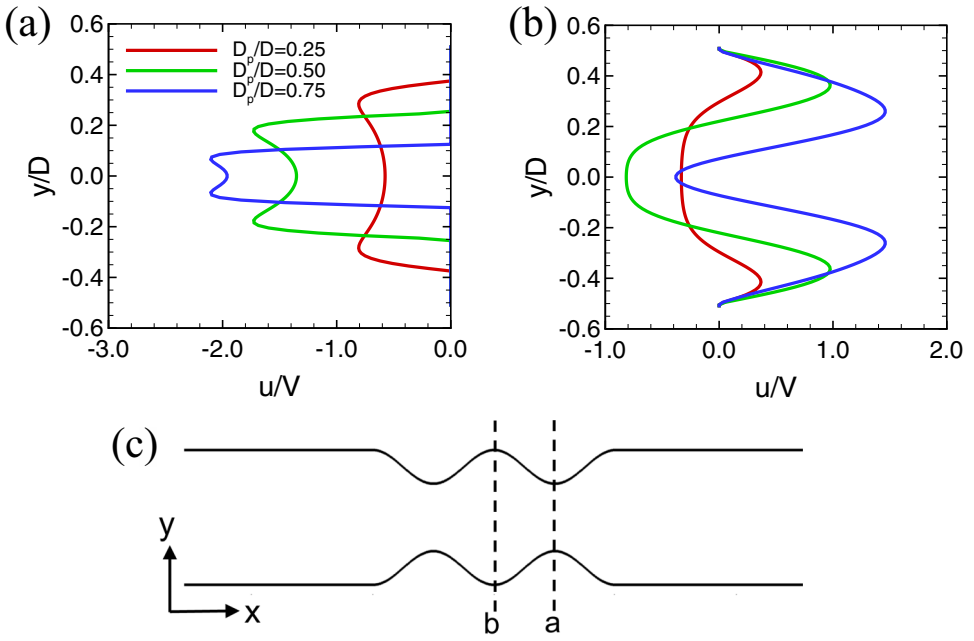

FIG. 5. The x-directional velocity profiles at (a) the most contracted region of the first wave ($x = x_{p,1} + Vt$), and (b) the widest region between the first and second waves $[x = (x_{p,1} + x_{p,2})/2 + Vt]$ for $N_p = 2$, $L/D = 15$, and $\lambda/D = 1$. Corresponding regions are shown in (c).

is the flow rate for $N_p = 1$. The flow rate increases with the number of peristaltic waves but is not proportional to the number of waves. In particular, for $D_p/D = 0.75$, the curve is far from the proportional line.

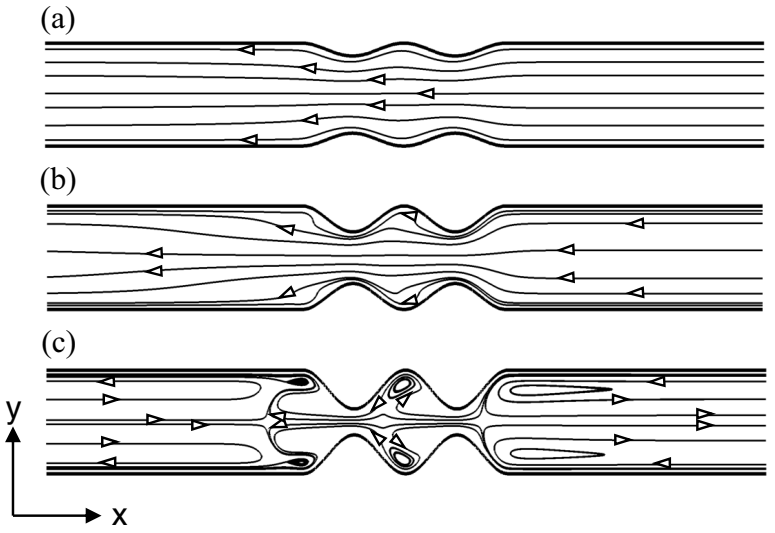

FIG. 6. Wave frame streamlines at the channel center (x-y cross section) for $N_p = 2$, $L/D = 15$, and $\lambda/D = 1$: (a) $D_p/D = 0.25$; (b) $D_p/D = 0.50$; (c) $D_p/D = 0.75$. Contracted regions are magnified.

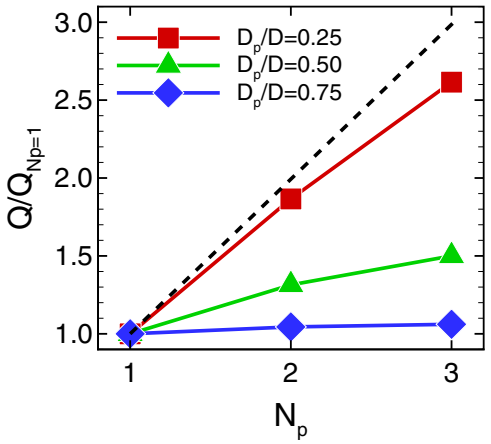

FIG. 7. Relationship between N_p and $Q/Q_{N_p=1}$, where $Q_{N_p=1}$ is the flow rate for $N_p = 1$. $L/D = 15$, and $\lambda/D = 1$. The dotted line represents the proportional line.

B. Pressure gradient generated by isolated contraction

To understand the underlying mechanism for flow rate produced by clustered contractions, we investigate an isolated contraction in channels with different channel lengths. Figure 8 shows the comparison of flow rates for different channel lengths where the flow rates are normalized by the flow rate at $L/D = 15$. The effect of the channel length on the flow rate becomes smaller for larger contraction ratios. Figure 9 shows the cross-sectional mean pressure along the direction of the channel length. For the small contraction ratio $D_p/D = 0.25$, the magnitude of the pressure gradient generated by the isolated contraction decreases with increasing L/D. For the large contraction ratio $D_p/D = 0.75$, however, such a decrease in the pressure gradient magnitude becomes small. These results suggest that the magnitude of pressure gradient produced by an isolated contraction does not decrease largely with increasing the channel length, minimizing a decrease in flow rate, in particular, for large contraction ratios.

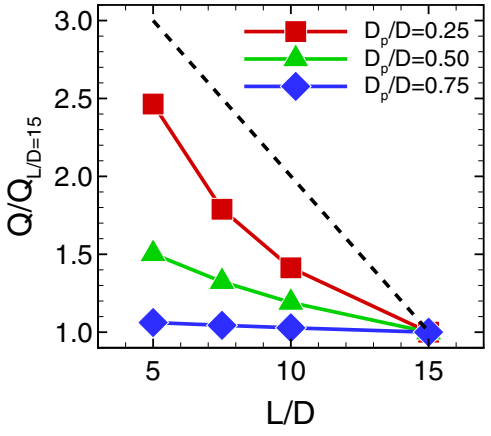

FIG. 8. Effect of channel length on flow rate for isolated contraction ($N_p = 1$), where $Q_{L/D=15}$ is the flow rate for $L/D = 15$.

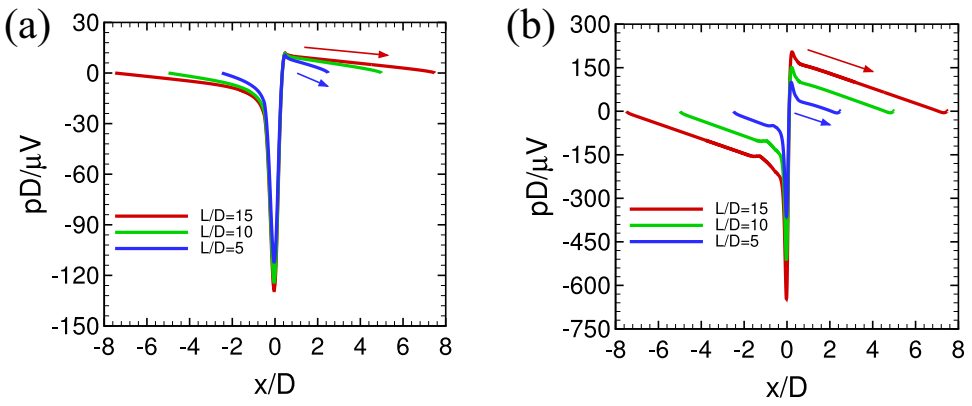

FIG. 9. Cross-sectional mean pressure along the channel for (a) $D_p/D = 0.25$ and (b) $D_p/D = 0.75$. Peristaltic wave is located at $x = 0$. Arrows indicate pressure gradient produced by contractions.

C. Relationship between isolated and clustered contractions

The numerical results in the previous section also suggest that the channel length per peristaltic wave is an important parameter determining flow rate. We compare the cross-sectional mean pressure distributions for three cases: $N_p = 1$ with $L/D = 5$, $N_p = 2$ with $L/D = 10$, and $N_p = 3$ with $L/D = 15$ for $D_p/D = 0.5$. In Fig. 10, we plot the normalized pressure $pD^2/\mu VL$ along the channel x/L. As expected, the pressure gradient of the three cases is nearly the same. Similar results are also obtained from the other contraction ratios. We, therefore, introduce the channel length per peristaltic wave L/N_pD.

Flow rates produced by clustered contractions of various values of N_p and L/D are plotted as a function of the channel length per wave in Fig. 11 where the flow rates are normalized by $Q_{\max} = S_{\max}V$, and $S_{\max}$ is the projected cross-sectional area at the most contracted region,

$$S_{\max} = \pi\left(\frac{D}{2}\right)^2 - \pi\left(\frac{D}{2} - \frac{D_p}{2}\right)^2 = \frac{\pi}{4}\left(2DD_p - D_p^2\right). \tag{13}$$

We also plot flow rates of periodic contractions of $\lambda/D = 1$, corresponding to $L/N_pD = 1$. We find that all the flow rates collapse onto a single curve of each contraction ratio. This result indicates that increasing the number of peristaltic waves in a cluster simply corresponds to decreasing the channel length per wave. In addition, we find that the flow rates of the clustered contractions converge to the flow rate of the periodic contractions. Note that the same tendency is found for the other Reynolds numbers $\mathrm{Re} < 10^2$.

The slopes of the flow rates are different for the contraction ratios. This is associated with the difference in the pressure gradient response to the channel length shown in Fig. 9. This also results in a nonproportional increase in flow rate with the number of waves in a cluster shown in Fig. 7.

D. Clustered contractions with different contraction ratios

In the previous sections, we have only considered the cluster of peristaltic waves with an identical shape. We now investigate the effect of the contraction ratio of the second wave for $N_p = 2$. The contraction ratios of the first and second waves are denoted by D_{p1} and D_{p2}, respectively, where $D_{p2}/D_{p1} = 0$ represents an isolated wave, and $D_{p2}/D_{p1} = 1$ is clustered waves with an identical shape. The relationship between D_{p2}/D_{p1} and $Q/Q_{\max}$ are shown in Fig. 12. The effect of the second wave on the flow rate depends on the contraction ratio of the first wave. For the small contraction

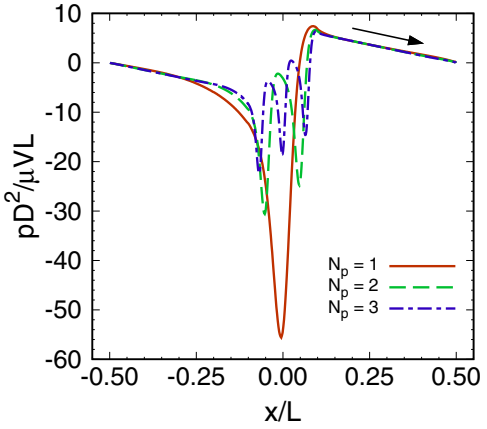

FIG. 10. Comparison of the cross-sectional mean pressure distribution for three cases: $N_p = 1$ with $L/D = 5$, $N_p = 2$ with $L/D = 10$ and $N_p = 3$ with $L/D = 15$ where the position and pressure are normalized as x/L and $pD^2/\mu VL$, respectively. Arrow indicates pressure gradient.

ratio of the first wave $D_{p1}/D = 0.25$, $Q/Q_{\max}$ increases with D_{p2}/D_{p1}. When the contraction ratio of the first wave is large, $Q/Q_{\max}$ does not increase with D_{p2}/D_{p1} until D_{p2}/D_{p1} exceeds a certain value. When $D_{p1}/D = 0.5$, the flow rate is nearly constant for $D_{p2}/D_{p1} < 0.4$, and when $D_{p1}/D = 0.75$, it is constant for $D_{p2}/D_{p1} < 0.7$.

E. Comparison to $\lambda/D \to \infty$ and $\mathrm{Re} \to 0$

We now compare the characteristics of peristaltic flow for $\lambda/D = 1$ and $\mathrm{Re} = 10^2$ to those for $\lambda/D \to \infty$ and $\mathrm{Re} \to 0$. We obtain the analytical solution of clustered contractions from the lubrication theory [10] as

$$\frac{Q}{D^2V} = \frac{\pi}{4}\left\{1 - \frac{I_1 + 2\pi\left(\frac{L}{N_p\lambda} - 1\right)}{I_2 + 2\pi\left(\frac{L}{N_p\lambda} - 1\right)}\right\}, \tag{14}$$

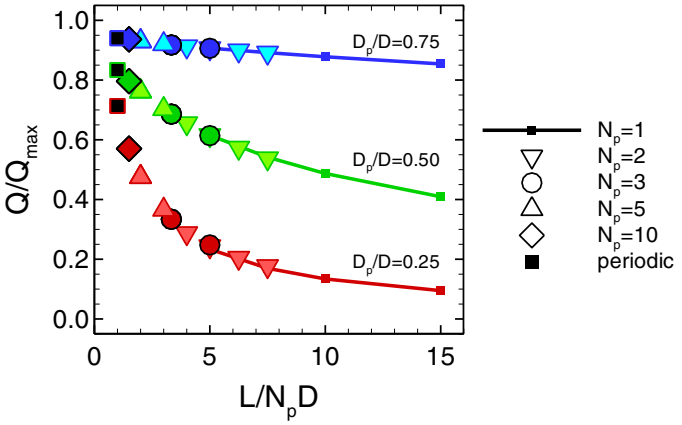

FIG. 11. Flow rate $Q/Q_{\max}$ as a function of the channel length per wave. Black square symbols represent flow rates of periodic contractions.

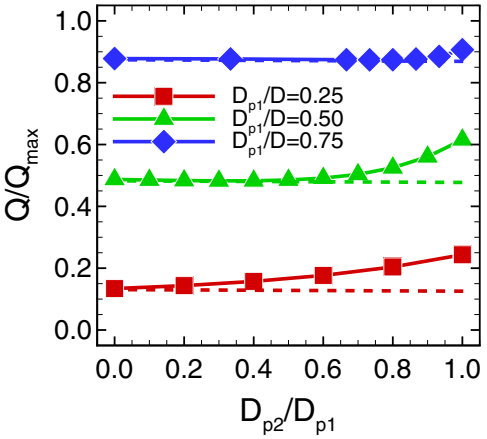

FIG. 12. Effect of the contraction ratio of the second wave on flow rate, where D_{p1} and D_{p2} denote the contraction ratios of the first and second waves, respectively.

where

$$I_1 = \pi \frac{(2-\phi)}{(1-\phi)^{3/2}}, \quad I_2 = \pi \frac{(2-\phi)(5\phi^2 - 8\phi + 8)}{8(1-\phi)^{7/2}}, \quad \phi = \frac{D_p}{D}, \tag{15}$$

and see the Appendix for details.

The lubrication theory assumes parabolic velocity profiles at any cross sections of the channel. However, the peristaltic flow for $\lambda/D \to \infty$ and $\mathrm{Re} \to 0$ has the characteristics of flow rate similar to $\lambda/D = 1$ and $\mathrm{Re} = 10^2$. The flow rate is not proportional to the number of waves in a cluster, and the flow rates of different numbers of waves collapse onto a single curve of each contraction ratio because of the same magnitude of the pressure gradient as shown in Fig. 13, where λ is used instead of D for the characteristics length of the problem.

For periodic waves with $\mathrm{Re} \to 0$ and $\lambda/D \to \infty$, Shapiro *et al.* [10] showed that the particle reflux in which fluid tracer particles move to the opposite direction of the peristaltic waves on average, occurs under negative pressure drop between the waves. Li and Brasseur [14] showed that the particle reflux for an isolated expansion wave is larger than that for periodic waves. They also reported that by contrast to the periodic waves, the particle reflux of the isolated expansion wave occurs even under no pressure drop between both the ends of the channel. Here, we present how tracer particles are transported by isolated and periodic contraction waves for $\lambda/D = 1$.

Figure 14 shows the trajectory of ten fluid tracer particles for $D_p/D = 0.5$. For an isolated contraction wave at $\mathrm{Re} = 10^{-1}$ [Fig. 14(a)], particles are transported to the downstream side without particle reflux as opposed to an isolated expansion wave [14]. Because of zero pressure drop between the inlet and the outlet of the channel as expected, no particle reflux also occurs for periodic contraction waves [Fig. 14(b)]. At $\mathrm{Re} = 10^2$, although particle trajectories are different from $\mathrm{Re} = 10^{-1}$ due to the inertia, again no particle reflux occurs for both the isolated and periodic contraction waves [Figs. 14(c) and 14(d)]. The particle travel distance along x direction l_x for five wave periods is presented in Fig. 15, where $l_x/\lambda = 5$ means that particles are trapped (i.e., transported with the same velocity as the waves). More than 10% of particles are trapped by the periodic contraction waves at $\mathrm{Re} = 10^{-1}$. Such trapped particles disappear either when the waves are isolated or when the Reynolds number increases to $\mathrm{Re} = 10^2$. The presence of inertia decreases the average travel distance for the clustered contractions (2.85 ± 1.57 for $\mathrm{Re} = 10^{-1}$ vs 1.82 ± 0.75 for $\mathrm{Re} = 10^2$) but does not change (or slightly increases) the travel distance for the isolated contraction (1.15 ± 0.58 for $\mathrm{Re} = 10^{-1}$ vs 1.24 ± 0.70 for $\mathrm{Re} = 10^2$).

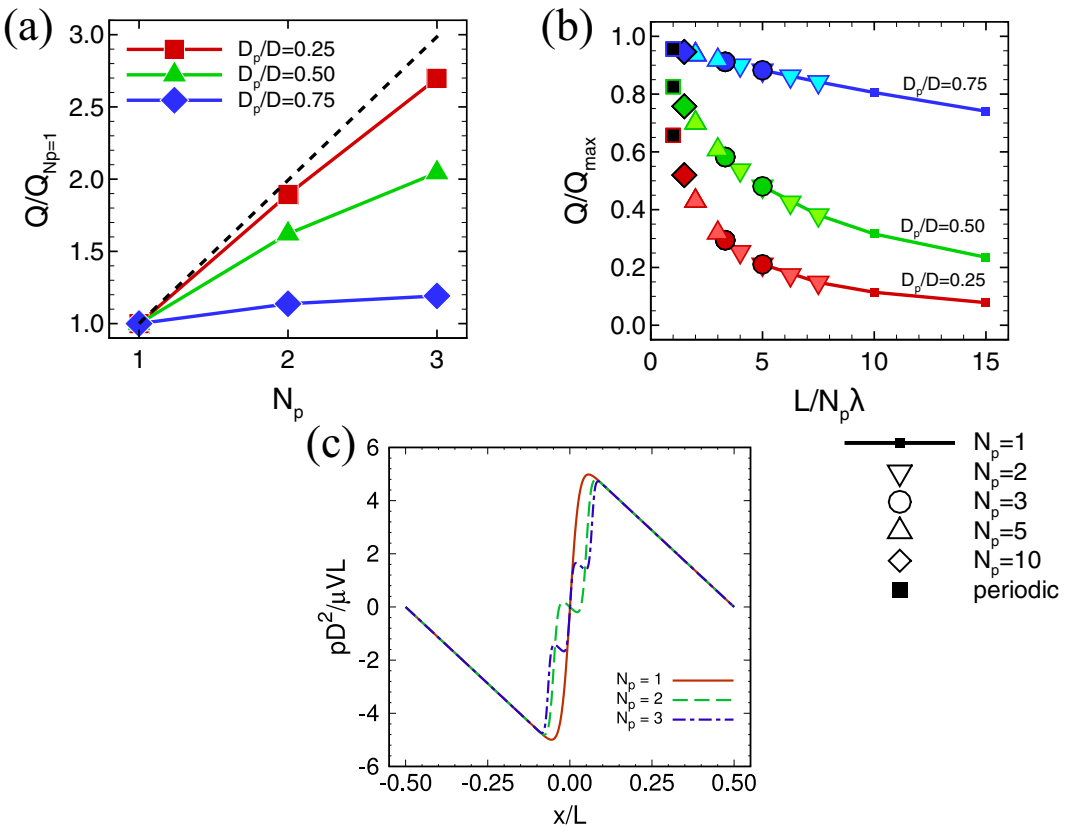

FIG. 13. Analytical solution for Re $\to 0$ and $\lambda/D \to \infty$. (a) Relationship between N_p and $Q/Q_{N_p=1}$. (b) Flow rate $Q/Q_{\max}$ as a function of $L/N_p\lambda$. (c) Comparison of the cross-sectional mean pressure distribution for three cases: $N_p = 1$–3 with $L/N_p\lambda = 5$.

IV. CONCLUSIONS

We have presented a numerical analysis of liquid flow produced by the cluster of peristaltic contractions in a circular channel for a finite Reynolds number Re $\sim 10^2$ and a finite contraction width $\lambda/D \sim 1$. Clustered contractions caused retrograde flow over the cluster and fluid trapping in the downstream and upstream regions of the cluster. Flow rate did not increase proportionally to the number of peristaltic waves in a cluster. To understand the underlying mechanism, we simulated flow produced by an isolated contraction in channels with different channel lengths. Pressure gradient did not decrease largely with increasing the channel length. When flow rates produced by various clustered contractions were plotted as a function of the channel length per peristaltic wave, the flow rates collapsed onto a single curve of each contraction ratio. In addition, we find that the flow rates of the clustered contractions converge to the flow rates of periodic contractions. We also show that the same characteristics of the flow rate are hold for Re $\to 0$ and $\lambda/D \to \infty$.

In the human body, clustered contractions consist of three–ten peristaltic waves. The Reynolds number can reach Re $\sim 10^2$ for low viscosity contents, and the wavelength of peristalsis may be comparable to the intestinal diameter. Our results provide the relationship among the flows produced by isolated, clustered, and periodic contractions for a wide range of Re and λ, and, thus, the results can be applied to a variety of physiological situations. We hope that this paper will help further understandings of gastrointestinal physiology and diseases.

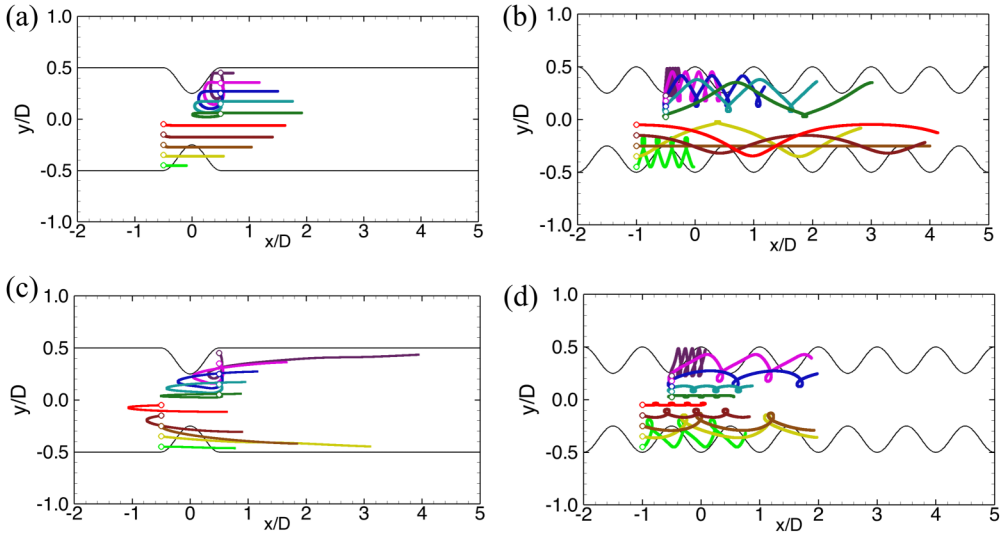

FIG. 14. Trajectories of ten tracer particles for five wave periods, where $\lambda/D = 1$ and $D_p/D = 0.5$. (a) isolated and (b) periodic contraction waves at $\mathrm{Re} = 10^{-1}$, (c) isolated, and (d) periodic contraction waves at $\mathrm{Re} = 10^{2}$. The initial position of particles are shown by circles. The particles are initially located at both the sides of the isolated wave (a) and (c) and at the most contracted and the widest regions for the clustered waves (b) and (d). The initial positions of the waves are also shown.

ACKNOWLEDGMENTS

This work was supported by Japan Society for the Promotion of Science (JSPS) KAKENHI Grants No. 17H02075 and No. 18K18817.

APPENDIX: ANALYTICAL SOLUTION FOR $\lambda/D \to \infty$ AND $\mathrm{Re} \to 0$

For $\lambda/D \to \infty$ and $\mathrm{Re} \to 0$, the Navier-Stokes equation may be written by

$$\frac{dp}{dx} = \frac{\mu}{r}\frac{\partial}{\partial r}\left(r\frac{\partial v}{\partial r}\right), \tag{A1}$$

where v is the fluid velocity at the wave frame and r is the radial position. Using the boundary conditions,

$$\begin{aligned} \frac{\partial v}{\partial r} &= 0 \quad \text{at} \quad r = 0, \\ v &= -V \quad \text{at} \quad r = h, \end{aligned} \tag{A2}$$

we have a parabolic velocity profile as

$$v = -V - \frac{R^2}{4\mu}\frac{dp}{dx}\left\{\left(\frac{h}{R}\right)^2 - \left(\frac{r}{R}\right)^2\right\}, \tag{A3}$$

where $R = D/2$ is the channel radius, and

$$h = \begin{cases} R & \left(-\frac{L}{2} \leqslant x \leqslant -\frac{N_p\lambda}{2},\ \frac{N_p\lambda}{2} \leqslant x \leqslant \frac{L}{2}\right), \\ R - \frac{D_p}{4}\left\{1 + \cos\frac{2\pi}{N_p\lambda}\left(x - \frac{L}{2}\right)\right\} & \left(-\frac{N_p\lambda}{2} \leqslant x \leqslant \frac{N_p\lambda}{2}\right), \end{cases} \tag{A4}$$

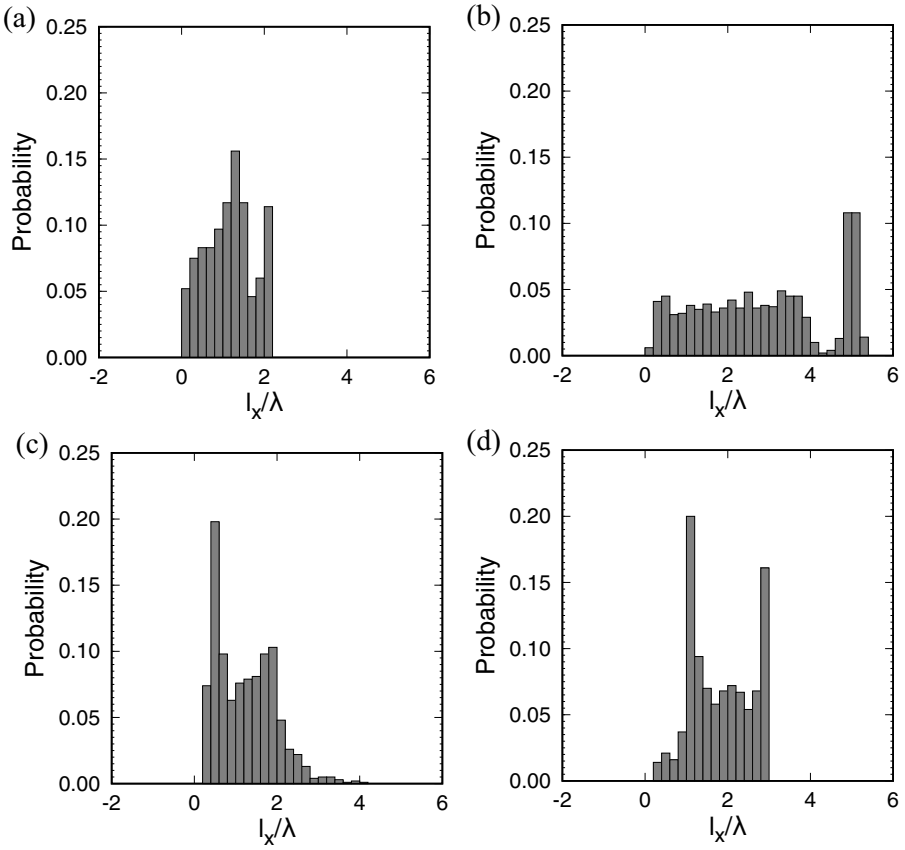

FIG. 15. Particle travel distance for five wave periods, where $\lambda/D = 1$ and $D_p/D = 0.5$. (a) isolated, (b) periodic contraction waves at $\mathrm{Re} = 10^{-1}$, (c) isolated, and (d) periodic contraction waves at $\mathrm{Re} = 10^{2}$. Some 1000 particles are initially located at random positions within $-1.5D < x < 1.5D$ on the x-y plane.

is the wall position. The volume flow rate at the wave frame is defined by

$$\begin{aligned} q &= \int_0^h 2\pi r v \, dr \\ &= -\pi V h^2 - \frac{\pi}{8\mu}\frac{dp}{dx}h^4, \end{aligned} \tag{A5}$$

and the pressure gradient is then

$$\frac{dp}{dx} = -8\mu V \frac{1}{h^2} - \frac{8\mu q}{\pi}\frac{1}{h^4}. \tag{A6}$$

The pressure rise in the straight region of the channel is given by

$$\begin{aligned} \Delta p_{\mathrm{straight}} &= \int_{-L/2}^{-(N_p\lambda/2)} \frac{dp}{dx} dx \\ &= \int_{N_p(\lambda/2)}^{L/2} \frac{dp}{dx} dx \\ &= \left(-8\mu V \frac{1}{R^2} - \frac{8\mu q}{\pi}\frac{1}{R^4}\right)\left(\frac{L}{2} - \frac{N_p\lambda}{2}\right), \end{aligned} \tag{A7}$$

and that in the wave region is

$$\Delta p_{\text{wave}} = \int_{-(N_p\lambda/2)}^{N_p\lambda/2} \frac{dp}{dx} dx$$
$$= -\frac{4\mu V N_p \lambda}{\pi R^2}\left(I_1 + \frac{q}{\pi R^2 V} I_2\right), \tag{A8}$$

where

$$I_1 = \pi \frac{(2-\phi)}{(1-\phi)^{3/2}}, \qquad I_2 = \pi \frac{(2-\phi)(5\phi^2 - 8\phi + 8)}{8(1-\phi)^{7/2}}, \qquad \phi = \frac{D_p}{D}. \tag{A9}$$

There is no pressure difference between the inlet and the outlet,

$$2\,\Delta p_{\text{straight}} + \Delta p_{\text{wave}} = 0, \tag{A10}$$

and the wave frame flow rate q is constant over the channel. Substituting Eqs. (A7) and (A8) into Eq. (A10), we have

$$q = -\pi V R^2 \frac{I_1 + 2\pi\left(\frac{L}{N_p\lambda} - 1\right)}{I_2 + 2\pi\left(\frac{L}{N_p\lambda} - 1\right)}. \tag{A11}$$

The flow rate at the stationary frame in the straight region is then given by

$$Q = \int_0^R 2\pi r(v + V) dr$$
$$= q + \pi V R^2$$
$$= \pi V R^2 \left\{1 - \frac{I_1 + 2\pi\left(\frac{L}{N_p\lambda} - 1\right)}{I_2 + 2\pi\left(\frac{L}{N_p\lambda} - 1\right)}\right\}. \tag{A12}$$

[1] H. J. Ehrlein and M. Schemann, *Gastrointestinal Motility* (Technische Universität München, Munich, Germany, 2005).

[2] A. M. Madrid, J. Poniachik, R. Quera, and C. Defilippi, Small intestinal clustered contractions and bacterial overgrowth: A frequent finding in obese patients, Dig. Dis. Sci. **56**, 155 (2011).

[3] R. W. Summers, S. Anuras, and J. Green, Jejunal manometry patterns in health, partial intestinal obstruction, and pseudoobstruction, Gastroenterology **85**, 1290 (1983).

[4] J. E. Kellow and S. F. Phillips, Altered small bowel motility in irritable bowel syndrome is correlated with symptoms, Gastroenterology **92**, 1885 (1987).

[5] M. Pimentel, E. E. Soffer, E. J. Chow, Y. Kong, and H. C. Lin, Lower frequency of mmc is found in ibs subjects with abnormal lactulose breath test, suggesting bacterial overgrowth, Dig. Dis. Sci. **47**, 2639 (2002).

[6] C. Tana, Y. Umesaki, A. Imaoka, T. Handa, M. Kanazawa, and S. Fukudo, Altered profiles of intestinal microbiota and organic acids may be the origin of symptoms in irritable bowel syndrome, Neurogastroenterol Motil. **22**, 512 (2010).

[7] S. Fukudo, T. Nomura, M. Muranaka, and F. Taguchi, Brain-gut response to stress and cholinergic stimulation in irritable bowel syndrome. a preliminary study. J. Clin. Gastroenterol. **17**, 133 (1993).

[8] V. Annese, G. Bassotti, G. Napolitano, P. Usai, A. Andriulli, and G. Vantrappen, Gastrointestinal motility disorders in patients with inactive crohn's disease, Scand. J. Gastroenterol. **32**, 1107 (1997).

[9] D. C. Baumgart and W. J. Sandborn, Crohn's disease, Lancet **380**, 1590 (2012).

[10] A. H. Shapiro, M. Y. Jaffrin, and S. L. Weinberg, Peristaltic pumping with long wavelengths at low reynolds number, J. Fluid Mech. **37**, 799 (1969).

[11] M. Y. Jaffrin and A. H. Shapiro, Peristaltic pumping, Annu. Rev. Fluid Mech. **3**, 13 (1971).
[12] S. Takabatake and K. Ayukawa, Numerical study of two-dimensional peristaltic flows, J. Fluid Mech. **122**, 439 (1982).
[13] C. Pozrikidis, A study of peristaltic flow, J. Fluid Mech. **180**, 515 (1987).
[14] M. Li and J. G. Brasseur, Non-steady peristaltic transport in finite-length tubes, J. Fluid Mech. **248**, 129 (1993).
[15] K. Connington, Q. Kang, H. Viswanathan, A. Abdel-Fattah, and S. Chen, Peristaltic particle transport using the lattice boltzmann method, Phys. Fluids **21**, 053301 (2009).
[16] H. S. Lew, Y. C. Fung, and C. B. Lowenstein, Peristaltic carrying and mixing of chyme in the small intestine (an analysis of a mathematical model of peristalsis of the small intestine), J. Biomech. **4**, 297 (1971).
[17] M. Mishra and A. R. Rao, Peristaltic transport of a newtonian fluid in an asymmetric channel, Z. Angew. Math. Mech. Phys. ZAMP **54**, 532 (2003).
[18] T. Hayat and N. Ali, Effect of variable viscosity on the peristaltic transport of a newtonian fluid in an asymmetric channel, Appl. Math. Model. **32**, 761 (2008).
[19] R. K. Avvari, Effect of local longitudinal shortening on the transport of luminal contents through small intestine, Acta Mech. Sin. **35**, 45 (2019).
[20] M. D. Sinnott, P. W. Cleary, and S. M. Harrison, Peristaltic transport of a particulate suspension in the small intestine, Appl. Math. Model. **44**, 143 (2017).
[21] G. Hounnou, C. Destrieux, J. Desme, P. Bertrand, and S. Velut, Anatomical study of the length of the human intestine, Surg. Radiol. Anat. **24**, 290 (2002).
[22] S. J. Stryker, T. J. Borody, S. F. Phillips, K. A. Kelly, R. R. Dozois, and R. W. Beart Jr., Motility of the small intestine after proctocolectomy and ileal pouch-anal anastomosis. Ann. Surg. **201**, 351 (1985).
[23] T. Takahashi, Flow behavior of digesta and the absorption of nutrients in the gastrointestine, J. Nutr. Sci. Vitaminol. **57**, 265 (2011).
[24] S. Ishida, T. Miyagawa, G. O'Grady, L. K. Cheng, and Y. Imai, Quantification of gastric emptying caused by impaired coordination of pyloric closure with antral contraction: A simulation study, J. R. Soc. Interface **16**, 20190266 (2019).
[25] T. Miyagawa, Y. Imai, S. Ishida, and T. Ishikawa, Relationship between gastric motility and liquid mixing in the stomach, Am. J. Physiol. Gastrointest. Liver Physiol. **311**, G1114 (2016).
[26] R. Berry, T. Miyagawa, N. Paskaranandavadivel, P. Du, T. R. Angeli, M. L. Trew, J. A. Windsor, Y. Imai, G. O'Grady, and L. K. Cheng, Functional physiology of the human terminal antrum defined by high-resolution electrical mapping and computational modeling, Am. J. Physiol. Gastrointest. Liver Physiol. **311**, G895 (2016).
[27] T. H. H. Wang, T. R. Angeli, S. Ishida, P. Du, A. Gharibans, N. Paskaranandavadivel, Y. Imai, T. Miyagawa, T. L. Abell, G. Farrugia, L. K. Cheng, and G. O'Grady, The influence of interstitial cells of cajal loss and aging on slow wave conduction velocity in the human stomach, Physiol. Rep. **8**, e14659 (2021).
[28] T. Krüger, H. Kusumaatmaja, A. Kuzmin, O. Shardt, G. Silva, and E. M. Viggen, *The Lattice Boltzmann Method* (Springer, Berlin, 2017), Vol. 10.
[29] M. Geier, M. Schönherr, A. Pasquali, and M. Krafczyk, The cumulant lattice boltzmann equation in three dimensions: Theory and validation, Comput. Math. Appl. **70**, 507 (2015).
[30] D. Yu, R. Mei, L. Luo, and W. Shyy, Viscous flow computations with the method of lattice boltzmann equation, Prog. Aerosp. Sci. **39**, 329 (2003).
[31] S. Takabatake, K. Ayukawa, and A. Mori, Peristaltic pumping in circular cylindrical tubes: A numerical study of fluid transport and its efficiency, J. Fluid Mech. **193**, 267 (1988).